IEEE Photonics Journal
An IEEE Photonics Society Publication

Open Access

A Stray Current Sensor Based on an All-Side Cylindrical Spiral Fiber

Volume 9, Number 1, February 2017

Shao-Yi Xu
Fang-Fang Xing
Wei Li
Yu-Qiao Wang
Xiang-Hui Wang
Rui-Lin Wang

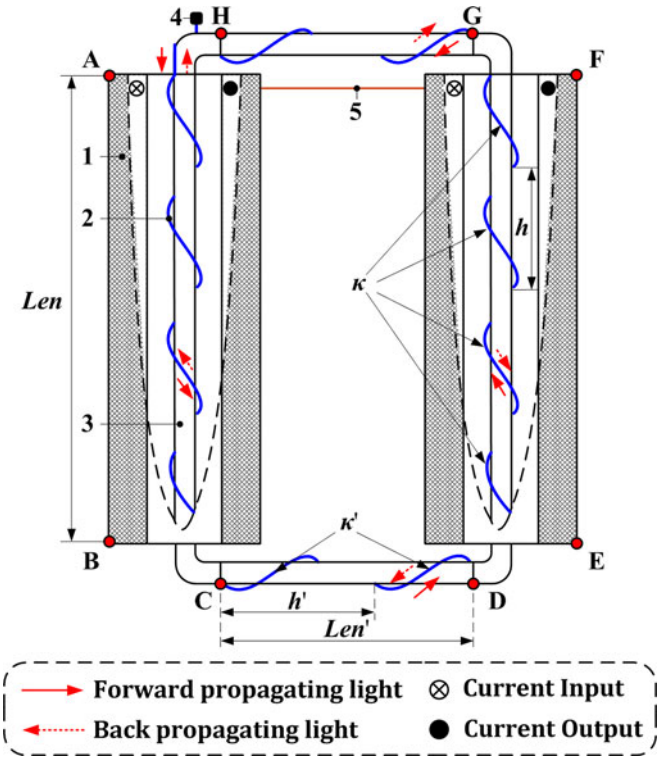

DOI: 10.1109/JPHOT.2016.2646365
1943-0655

A Stray Current Sensor Based on an All-Side Cylindrical Spiral Fiber

Shao-Yi Xu,[1,2] Fang-Fang Xing, Wei Li,[3] Yu-Qiao Wang,[1] Xiang-Hui Wang,[1] and Rui-Lin Wang[1]

[1]School of Mechanical and Electrical Engineering, China University of Mining and Technology, Xuzhou 221116, China
[2]Postdoctoral Station of Electrical Engineering, School of Information and Electrical Engineering, China University of Mining and Technology, Xuzhou 221116, China
[3]School of Mechatronic Engineering, Xuzhou College of Industrial Technology, Xuzhou 221116, China

DOI:10.1109/JPHOT.2016.2646365

Manuscript received October 12, 2016; revised December 23, 2016; accepted December 26, 2016. Date of publication December 29, 2016; date of current version January 19, 2017. This work was supported in part by the National Natural Science Foundation of China under Grant 51607178, in part by the China Postdoctoral Science Foundation under Grant 2015M581882, in part by the Jiangsu Planned Projects for Postdoctoral Research Funds under Grant 1601260C, in part by the Priority Academic Program Development of Jiangsu Higher Education Institutions, and in part by the Top-Notch Academic Programs Project of Jiangsu Higher Education Institutions. Corresponding author: Prof. Wei Li (e-mail: Prof_liwei@126.com)

Abstract: In this paper, a stray current sensor based on an all-side cylindrical spiral fiber is proposed. The configuration of stray current sensor is illustrated first. The Jones matrix of sensor head is derived based on the geometric rotation effect. The output representation of stray current sensor is also obtained. Moreover, the effect of the characteristic parameters of sensor head on the output error is evaluated. On these bases, the genetic algorithm is applied to optimize these characteristic parameters in the range of the temperature-induced linear birefringence from 0° to 1000°. The optimization results include the following: For the vertical side, the length of cylindrical rod and the number of curve spirals are 1024 mm and 35, respectively; for the horizontal side, these two parameters are 876 mm and 28, respectively. The temperature experiments are conducted to test the performance of the stray current sensor with reference to that without cylindrical spiral fiber, and the test results indicate that the measurement error of the proposed stray current sensor is not larger than 0.4%, which can be suited for the stray current measurement in an urban rail transit system.

Index Terms: Stray current sensor, geometric rotation effect, optimization.

1. Introduction

The optical fiber current sensor (OFCS) has been under investigation since the 1970s [1]. Its operation mainly depends on the Faraday effect in the single mode optical fiber [1]–[4]. The main benefits of OFCS are current measurement with high fidelity, high safety of operation, and environmental friendliness [5]. The other advantages of OFCS have been reported, such as high accuracy, wide dynamic range, wide bandwidth, and dielectric nature [6], [7]. The OFCS has been found to enter into applications in high voltage substations for electric power transmission [8], [9], current measurement for process control and protection in electrowinning industry [10], and current measurement for buried pipelines protection in an urban rail transit system [3]. The formal two applications maybe well know while the last one maybe not. In the last application, this described current of buried pipelines, such as the oil pipeline, water pipeline, and gas pipeline, is usually called stray current. Since the magnitude of stray current is closely related to the corrosion status of buried pipelines,

the measurement on stray current can provide a new method to evaluate the corrosion status [11], [12]. The stray current is known to produce from the DC traction current of the train along the running rail, which includes the primary stray current and the secondary one. The primary stray current can be captured by the stray current collection system, which has no effect on the buried pipeline. The secondary stray current enters the buried pipeline and then causes the electrolytic corrosion. According to our test results in a metro system, the secondary stray current on a single buried pipeline is proven to be a low frequency current, which is not greater than 10.94 Hz, and its magnitude is within the range from -19.3 A to 20.8 A.

The OFCS, which is the passive and anti-corrosion sensor, is an advantageous candidate to measure the secondary stray current. According to the signal detection method, the OFCS can be divided into two main types including interferometer [4], [7]–[8] and polarimetric [1]–[3], [5], [6]. Compared with the interferometer OFCS, the polarimetric OFCS has the advantages of simple optical structure and low cost. Thus, the polarimetric OFCS has been applied to measure stray current, which is called stray current sensor [3], [6]. During the practical applications, the main problem of the stray current sensor is the sensitivity to temperature, that is, the sensor performance may be declined due to the temperature-induced linear birefringence. As far as we know, two effective methods have been applied to solve the temperature-sensitive problem. The first method applies the thermally annealed fiber as the sensing fiber [13]. However, the thermally annealed fiber is found to be easily damaged. The other method applies the spun highly birefringent fiber as the sensing fiber [14], [15]. However, the Verdet constant of this spun highly birefringent fiber is difficult to be evenly distributed. Moreover, this fiber needs to be improved in some ways, such as the high cost of fabrication and the high polarization mode dispersion [16].

In this paper, first, we propose a stray current sensor based on an all-side cylindrical spiral fiber (CSF). In each side, it winds the sensing fiber along the cylindrical spiral curve, which produces the circular birefringence to suppress the linear birefringence based on geometric rotation effect. The configuration of stray current sensor is demonstrated, and a sensor head using all-side CSF is illustrated in detailed. The Jones matrix of the sensor head is then derived. Moreover, the output representation of stray current sensor is obtained. And the effect of the characteristic parameters of the sensor head on the output error is evaluated. On these bases, the genetic algorithm is applied to optimize the characteristic parameters, including the length of the cylindrical rod and the number of the curve spirals. Finally, comparing with the stray current sensors without CSF, the temperature experiments are conducted to assert the superiority of stray current sensor with all-side CSF.

2. Optical Configuration and Output Representation for Stray Current Sensor

The stray current sensor is composed of a super luminescent diode (SLD) source, a polarizer, a coupler, a sensor head, a polarization controller (PC), a polarization beam splitter (PBS) and an optical power meter (OPM), whose configuration is shown in Fig. 1. The sensor head is composed of the sensing fiber, two multilayer solenoids and a mirror. It is noted that the mirror is attached at the end of the sensing fiber. Firstly, the light from the SLD passes through the polarizer to form the linearly polarized light. The linearly polarized light then travels through the coupler and enters into the sensor head. During the sensor head, the linearly polarized light propagates in the sensing fiber and the plane of polarization is rotated due to the magnetic field induced by the stray current applied on the solenoids. The linearly polarized light is reflected by the mirror and passes the sensing fiber for a second time. Since the Faraday Effect is nonreciprocal, the rotation angle is double. The linearly polarized light from the sensor head is coupled into the PC that is used to modulate the plane of polarization through 45 degrees [3]. The modulation light travels into the PBS and then splits into the orthogonally optical signals that are detected by the OPM. Finally, the detection results of the OPM are sent to the industrial personal computer (IPC) by RS 232 interface.

The detailed configuration of the sensor head is shown in Fig. 2(a). The two solenoids are designed to connect in series through a conducting wire, which are installed in the sections AB and EF, respectively, which means that the magnetic field intensities are the same for the sensing

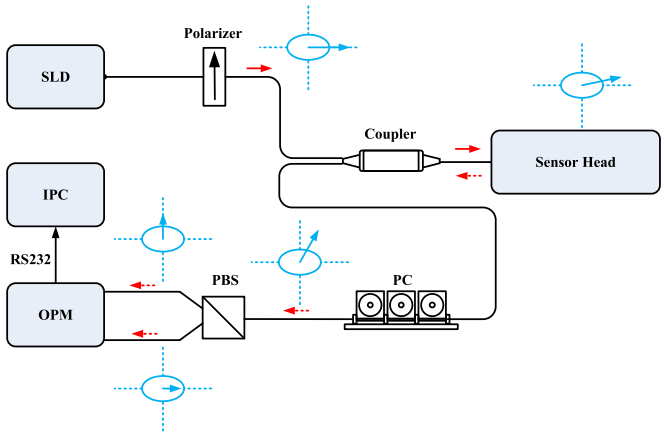

Fig. 1. Optical configuration of stray current sensor.

fiber in sections AB and EF. Moreover, the sensing fiber is installed on a cylindrical rod along a spiral curve in section AB, which is the same as the installations in sections CD, EF and GH. Thus, the sensing fiber is called as the all-side CSF. It is noted that the linear birefringence, the circular birefringence and the magnetic field work together on the CSF in section AB as well as in section EF. However, only the first two factors play a role on that in sections CD and GF. The parameters' distribution is shown in Fig. 2(b).

In section AB, the parameter equation of the CSF is expressed as

$$\rho(\alpha) = \rho_x \cdot \mathbf{i} + \rho_y \cdot \mathbf{j} + \rho_z \cdot \mathbf{k} = r\cos(\kappa\alpha) \cdot \mathbf{i} + r\sin(\kappa\alpha) \cdot \mathbf{j} + h(\kappa\alpha)/2\pi \cdot \mathbf{k} \tag{1}$$

where $0 \le \alpha \le 2\pi$, r is the radius of the cylindrical rod, κ is the number of the curve spirals, and h is the length of each curve spiral.

The magnetic field intensity along the CSF can be simplified as [3]

$$H = n_1 \cdot n_2 \cdot \frac{Len}{2} \cdot \ln\left[\left(b + \sqrt{b^2 + \frac{Len^2}{4}}\right) \Big/ \left(a + \sqrt{a^2 + \frac{Len^2}{4}}\right)\right] \cdot Cur \tag{2}$$

where the parameters a and b represent the internal and external diameter of multilayer solenoid, respectively. The parameter Len represents the length of multilayer solenoid. The parameter Cur represents the applied stray current. The parameters n_1 and n_2 are equal to num_1/Len and $num_2/(b\text{-}a)$, respectively. It is noted that num_1 and num_2 are defined as the number of turns along the axial and vertical direction of multilayer solenoid, respectively.

According to (1), the length of the CSF can be derived as

$$L = \int_0^{2\pi} \sqrt{(\rho_x' \mathrm{d}\alpha)^2 + (\rho_y' \mathrm{d}\alpha)^2 + (\rho_z' \mathrm{d}\alpha)^2} = \kappa \cdot \sqrt{4\pi^2 r^2 + h^2}. \tag{3}$$

Moreover, the torsion τ and curvature μ of the CSF are obtained as (4), respectively.

$$\tau = \frac{(\rho', \rho'', \rho''')}{(\rho' \times \rho'')^2} = \frac{2\pi h}{h^2 + 4\pi^2 r^2}; \mu = \frac{|\rho' \times \rho''|}{|\rho'|^3} = \frac{4\pi^2 r}{h^2 + 4\pi^2 r^2}. \tag{4}$$

In our sensor, the linear birefringence of the CSF may be induced by the bending stress or the thermal stress. Among them, the bending-induced linear birefringence (BLB) of the CSF per meter is given by [17]:

$$\beta_b = \frac{\pi n^3}{2\lambda}(p_{12} - p_{11})(1 + \nu) r_1^2 \cdot \mu^2. = 0.0021 \cdot \mu^2 \,(\mathrm{red/m}) \tag{5}$$

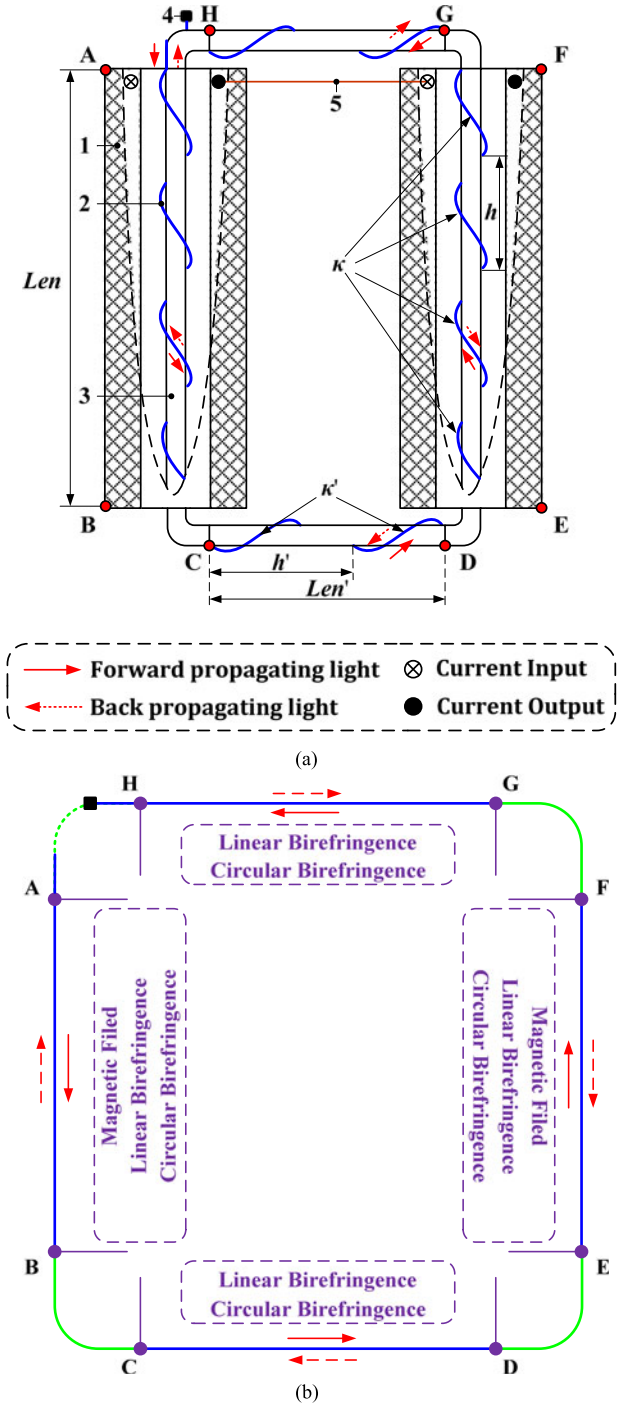

Fig. 2. Sensor head with all-side CSF and its parameters distribution: (a) Sensor head: 1. Multilayer solenoid; 2. Sensing fiber 3. Cylindrical rod; 4. Mirror; 5. Conducting wire. (b) Parameters' distribution.

where λ is the wavelength of the input light, $\lambda = 1.55$ um; n is the refractive index of the fiber core, $n = 1.458$; $p_{11,\ 12}$ are the strain-optical coefficients, $p_{11} = 0.121$ and $p_{12} = 0.270$; ν is the Poisson's ratio, $\nu = 0.17$; r_1 is the equivalent radius of the CSF, $r_1 = 62.5$ um. Moreover, the temperature-induced linear birefringence (TLB) of the CSF per meter is defined as β_t, which is difficult to be calculated like β_b at present. The main challenge is how to accurately obtain the

stress difference between the principal axes of the CSF when the temperature is changed. And there is no effective method to measure this stress difference of the meter-long CSF. In this work, the parameters optimization of the CSF is firstly performed within a preset range of the TLB. On this basis, the temperature experiment is used to evaluate the accuracy of this preset range. Thus, for the CSF, the linear birefringence is equal to βL, which is the sum of $\beta_b L$ and TLB, the circular birefringence is equal to τL [18], and the Faraday rotation angle is equal to VHL [6]. It is noted that V represents the Verdet constant of the CSF.

For the forward propagating light beam, the Jones matrix of the CSF is obtained as [19]

$$J_{fc} = \begin{bmatrix} \cos t + i\frac{\beta L}{2}\left(\frac{\sin t}{t}\right) & -(\tau L + VHL)\left(\frac{\sin t}{t}\right) \\ (\tau L + VHL)\left(\frac{\sin t}{t}\right) & \cos t - i\frac{\beta L}{2}\left(\frac{\sin t}{t}\right) \end{bmatrix}. \tag{6}$$

For the back propagating light beam, the Jones matrix of the CSF is obtained as [19]

$$J_{bc} = \begin{bmatrix} \cos w + i\frac{\beta L}{2}\left(\frac{\sin w}{w}\right) & -(\tau L - VHL)\left(\frac{\sin w}{w}\right) \\ (\tau L - VHL)\left(\frac{\sin w}{w}\right) & \cos w - i\frac{\beta L}{2}\left(\frac{\sin w}{w}\right) \end{bmatrix} \tag{7}$$

where

$$t = \sqrt{(\tau L + VHL)^2 + (\beta L/2)^2}$$

$$w = \sqrt{(\tau L - VHL)^2 + (\beta L/2)^2}.$$

For the CSF in section CD, the length of the cylindrical rod and the number of the curve spirals are both different from the CSF in section AB. In addition, the CSF in section CD is irrelevant to the magnetic field induced by the applied stray current. Thus, for the forward and back propagating light beam, the Jones matrices of the CSF in section CD are derived as

$$J_{fv} = J_{bv} = \begin{bmatrix} \cos v + i\frac{\beta' L'}{2}\left(\frac{\sin v}{v}\right) & -\tau' L'\left(\frac{\sin v}{v}\right) \\ \tau' L'\left(\frac{\sin v}{v}\right) & \cos v - i\frac{\beta' L'}{2}\left(\frac{\sin v}{v}\right) \end{bmatrix} \tag{8}$$

where

$$v = \sqrt{(\tau' L')^2 + (\beta' L'/2)^2}.$$

The parameters L', τ' and μ' represent the length, the torsion, and the curvature for the CSF in section CD, which are obtained based on (3) to (4). The parameter β'L' represents the linear birefringence for the CSF in section CD, which can be obtained by reference to the βL. Moreover, the length of cylindrical rod and the number of curve spirals are defined as Len' and κ', respectively.

The Jones matrices of the CSF in section EF are the same as that in section AB. And the Jones matrices of the CSF in section GH are the same as that in section CD. Thus, according to (6) to (8), the Jones matrix of the sensor head can be derived as

$$J_s = \underbrace{\underbrace{J_{bc}J_{bv}J_{bc}J_{bv}}_{\text{The first turn}} \cdots \underbrace{J_{bc}J_{bv}J_{bc}J_{bv}}_{\text{The } N\text{th turn}}}_{\text{Back Propagation}} \cdot J_m \cdot \underbrace{\underbrace{J_{fv}J_{fc}J_{fv}J_{fc}}_{\text{The } N\text{th turn}} \cdots \underbrace{J_{fv}J_{fc}J_{fv}J_{fc}}_{\text{The first turn}}}_{\text{Forward Propagation}} \tag{9}$$

where J_m represents the Jones matrix of the mirror.

When the applied stray current is equal to 0 A, the Jones matrix of the sensor head is defined as J_{s0}, which is the special case of (9). In this case, the Jones vector of the output signal from the PBS is defined as E_s. Moreover, when the applied stray current is not equal to 0 A, the Jones vector of the output signal from the PBS is defined as E_d. The vectors E_s and E_d can be given by

$$E_s = J_{pc} \cdot J_{s0} \cdot J_p \cdot E_i;\ E_d = J_{pc} \cdot J_s \cdot J_p \cdot E_i \tag{10}$$

where J_p represents the Jones matrix of the polarizer, and J_{pc} represents the Jones matrix of the PC; E_i is the Jones vector of the light beam from the SLD source.

Compared with [20], a quadrature processing is improved for the output signal. An actual output (AO) and independent of the input optical power is obtained as

$$\mathrm{AO} = \frac{(P_{dx} - P_{sx}) - (P_{dy} - P_{sy})}{P_{sx} + P_{sy}} = \frac{\left[E_d(1)\,E_d(1)^* - E_s(1)\,E_s(1)^*\right] - \left[E_d(2)\,E_d(2)^* - E_s(2)\,E_s(2)^*\right]}{E_s(1)\,E_s(1)^* + E_s(2)\,E_s(2)^*} \tag{11}$$

3. Parameter Optimization of Sensor Head

The known parameters of our sensor head include $n_1 = 639.7/\mathrm{m}$; $n_2 = 545.2/\mathrm{m}$; $a = 32\,\mathrm{mm}$; $b = 54\,\mathrm{mm}$; $r = 2\,\mathrm{mm}$; $V = 0.804\,\mathrm{urad/A}$, and the unknown parameters include *Len*, *Len*', κ and κ'. It is noted that the lengths of each curve spiral h and h' are equal to *Len*/κ and *Len*'/κ' in sections AB and CD, respectively. Obviously, these unknown parameters are critical for the output error reduction. According to [7], the current must be measured with accuracy to within $\pm 0.2\%$ in the electricity metering applications and $\pm 1\%$ for substation protection purposes. However, there have been no standards for referencing in determining the accuracy for stray current measurement. According to Faraday's law of electrolysis [21], the corrosion amount of buried pipeline is about 2354.5 g at 1 A stray current in a year (about 365 days). In practice, the corrosion status of the buried pipeline can be accurately determined when the corrosion amount reaches 2345.1 g. Thus, the stray current measurement accuracy should be controlled within $\pm 0.4\%$.

If the linear birefringence is completely suppressed by the circular birefringence produced from CSF, the Jones matrices of the sensor head with and without the applied stray current will be given by

$$J_l = \begin{bmatrix} -\cos(2VHL) & \sin(2VHL) \\ \sin(2VHL) & \cos(2VHL) \end{bmatrix}; J_{l0} = \begin{bmatrix} -1 & 0 \\ 0 & 1 \end{bmatrix}. \tag{12}$$

Thus, the desired output (DO) of stray current sensor can be derived as

$$\mathrm{DO} = \frac{\left[E_{ld}(1)\,E_{ld}(1)^* - E_{ls}(1)\,E_{ls}(1)^*\right] - \left[E_{ld}(2)\,E_{ld}(2)^* - E_{ls}(2)\,E_{ls}(2)^*\right]}{E_{ls}(1)\,E_{ls}(1)^* + E_{ls}(2)\,E_{ls}(2)^*} \tag{13}$$

where $E_{ls} = J_{pc} \cdot J_{l0} \cdot J_p \cdot E_i$ and $E_{ld} = J_{pc} \cdot J_l \cdot J_p \cdot E_i$. In addition, the output error (OE) can be derived based on (11) and (13), which is given by

$$\mathrm{OE} = \left| \frac{\mathrm{AO} - \mathrm{DO}}{\mathrm{DO}} \right| \times 100\%. \tag{14}$$

Two simulations have been conducted to demonstrate the relationship between the OE and the unknown parameters, that is, *Len*, *Len*', κ and κ'. The applied current is set as 20 A during the two simulations. In the first simulation, these four unknown parameters are set as 700 mm, 650 mm, 13 and 9, respectively. For the CSF in section AB, the same goes for that in section EF, the BLB is about 15.3 deg based on (5), respectively. And the BLB is about 4.4 deg for that in sections CD and GH. In the second simulation, the four unknown parameters are set as 900 mm, 700 mm, 11 and 14, respectively. The BLB are about 3.7 deg in sections AB and EF. And the BLB is about 20.5 deg in sections CD and GH. Moreover, during these two simulations, the TLB is set within the range from 0 deg to 1000 deg for each section, which may induced by the BLB variation as the temperature changes or the expansion coefficient difference between the CSF and the cylindrical rod. The output error curves of these two simulations are shown in Fig. 3(a) and (b), respectively. In Fig. 3, the output error is found to be not larger than 0.4% within several limit ranges. For the first simulation, the range is between 0 deg and 306 deg. For the second simulation, the range is between 0 deg and 330 deg. However, the desired result is that the OE is smaller than 0.4% when the TLB is in the range from 0 deg to 1000 deg. These two simulations indicate that the

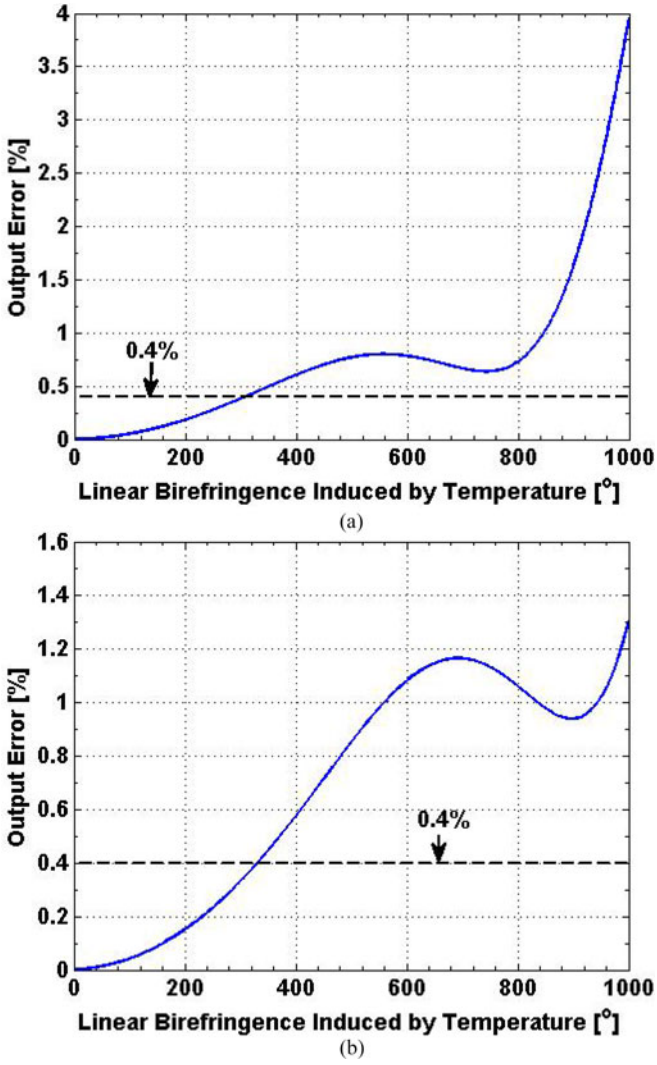

Fig. 3. Output error curves based on two simulations: 1. (a) *Len* = 700 mm, *Len*' = 650 mm, $\kappa = 13$ and $\kappa' = 9$. (b) *Len* = 900 mm, *Len*' = 700 mm, $\kappa = 11$ and $\kappa' = 14$.

unknown parameters have an important effect on the OE. Thus, the unknown parameters need to be optimized.

The genetic algorithm (GA) is applied to determine the optimal results of the unknown parameters in this work. In the GA, each individual in the population represents a possible solution of the unknown parameters, which is characterized by a 32-bit string of 0s or 1s. In each individual, the first 6 bits, the seventh to 12th bits, the 13th to 22th bits and the last 10 bits corresponds to κ, κ', *Len*, and *Len*', respectively. There are 80 individuals in the population. A fitness function is required to investigate what the fitness level is for each individual [22]. And the output error OE is set as the fitness function (Fit). The GA begins its evolution process from a random population. The evolution process is repeated a predetermined number of generations [23]; thereafter the GA stops and the optimal parameters can be determined from the final solution with the smallest OE. In each generation cycle, the population of solutions is subjected to the action of specially constructed genetic operators: selection, crossover, and mutation [24]. First, the selection process is based on probability, i.e., solutions evaluated with higher Fit values are most likely to be selected for the next generation, while those with low Fit values will most likely not survive. This work uses the roulette wheel scheme as the selection operator [23], [24]. Once the superior solutions have been

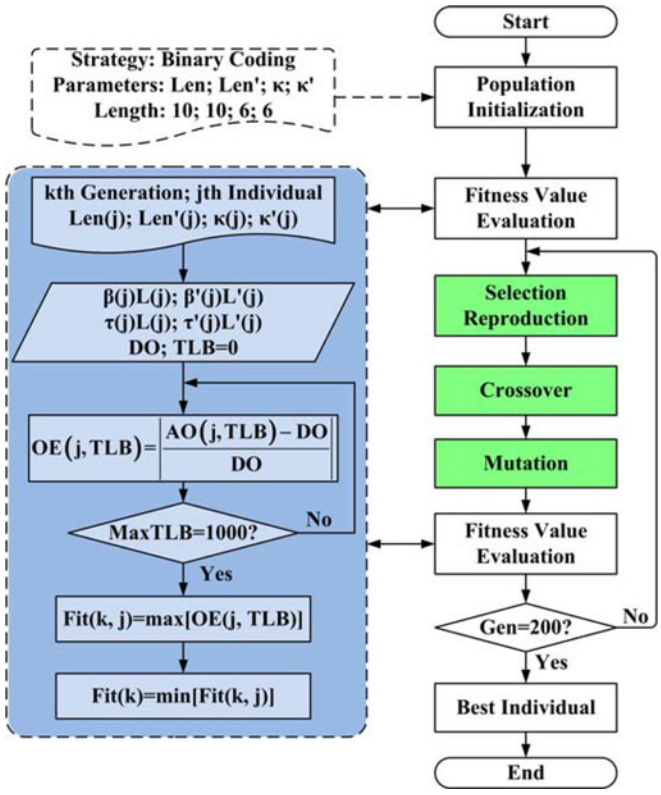

Fig. 4. Flowchart of parameters optimization based on genetic algorithm.

selected, the crossover process randomly chooses two selected solutions (i.e., parents), exchanges their bit information, and then generates two further solutions (i.e., offspring). This process is used to select the good genes accumulated from the parents' generation with the intention that these genes will produce even better individuals. Finally, if the GA relies simply on the crossover process to reproduce the offspring, the individual cannot evolve with the new feature [22]. The mutation process causes an existing individual to be modified and, hence, introduces an additional variability into the population [24]. This process helps to prevent the GA from getting trapped in a local optimal solution. The three operations will be iteratively performed in the GA process, and the GA process continues to evolve endlessly without setting termination conditions. Therefore, the termination condition is set to 200 evolutionary generations. The process flow for the GA used in our study is shown in Fig. 4, and the fitness function evaluation process is shown in the dotted box.

The evaluation process of genetic algorithm is shown in Fig. 5(a). And the Fit of the best individual is about 0.1644% in the maximum generation. After decoding the best individual, the optimized parameters are obtained, that is, *Len* = 1024 mm, *Len*' = 876 mm, $\kappa = 35$, and $\kappa' = 28$. In the range of TLB from 0 deg to 1000 deg, the OEs are all not larger than 0.4% shown in Fig. 5(b). It is found that the maximum OE is 0.1644% at 656 deg, which is consistent with the evaluation result. It indicates that the optimized results of genetic algorithm are accurate. Furthermore, the feasibility of these optimized results needs to be verified for other current, because these optimized results are obtained at 20 A. And the verification result is shown in Fig. 6. It is found that the OE is not larger than 0.4% within the range from 1 A to 20 A. For example, the maximum OE is found to be 0.2577% at 5 A, 0.2382% at 10 A, and 0.2077% at 15 A. It means that these optimized results are applicable to the whole measurement range of stray current sensor. Next, the stray current sensor will be fabricated based on these optimized results. Moreover, the temperature experiments will be conducted to test the performance of the optimized sensor.

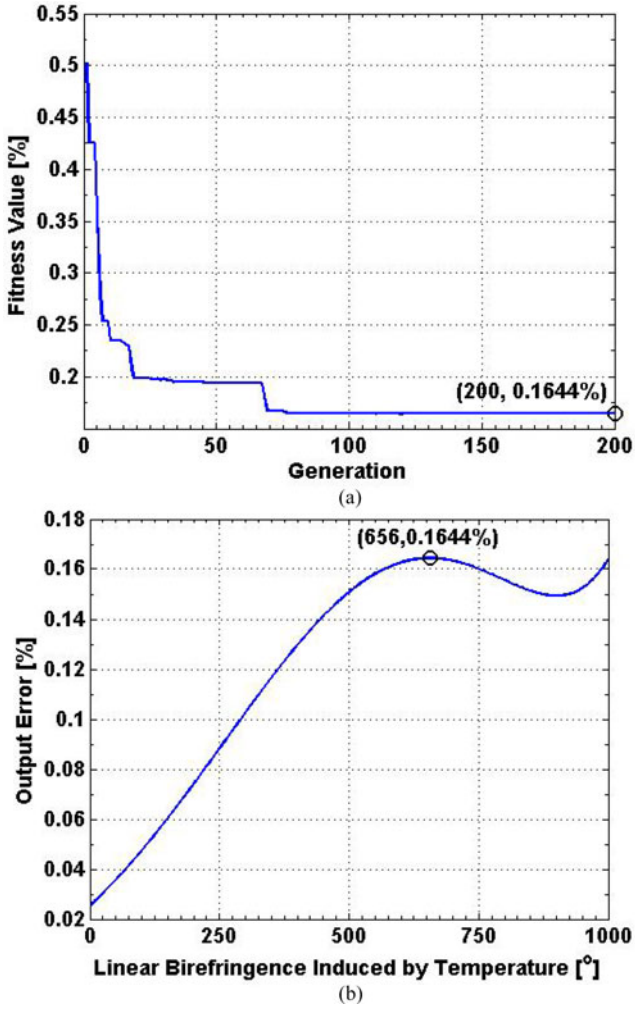

Fig. 5. Optimization results using genetic algorithm. (a) Evaluation process of genetic algorithm. (b) OE at 20A in the range of the TLB from 0 deg to 1000 deg based on the optimized parameters.

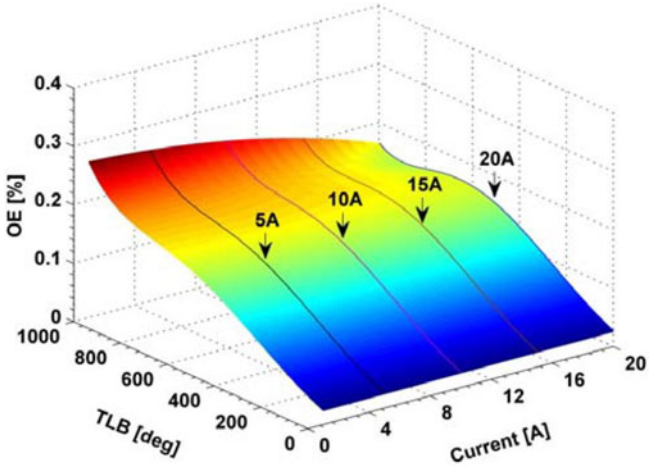

Fig. 6. Output error within the range of the experiment current from 1 A to 20 A.

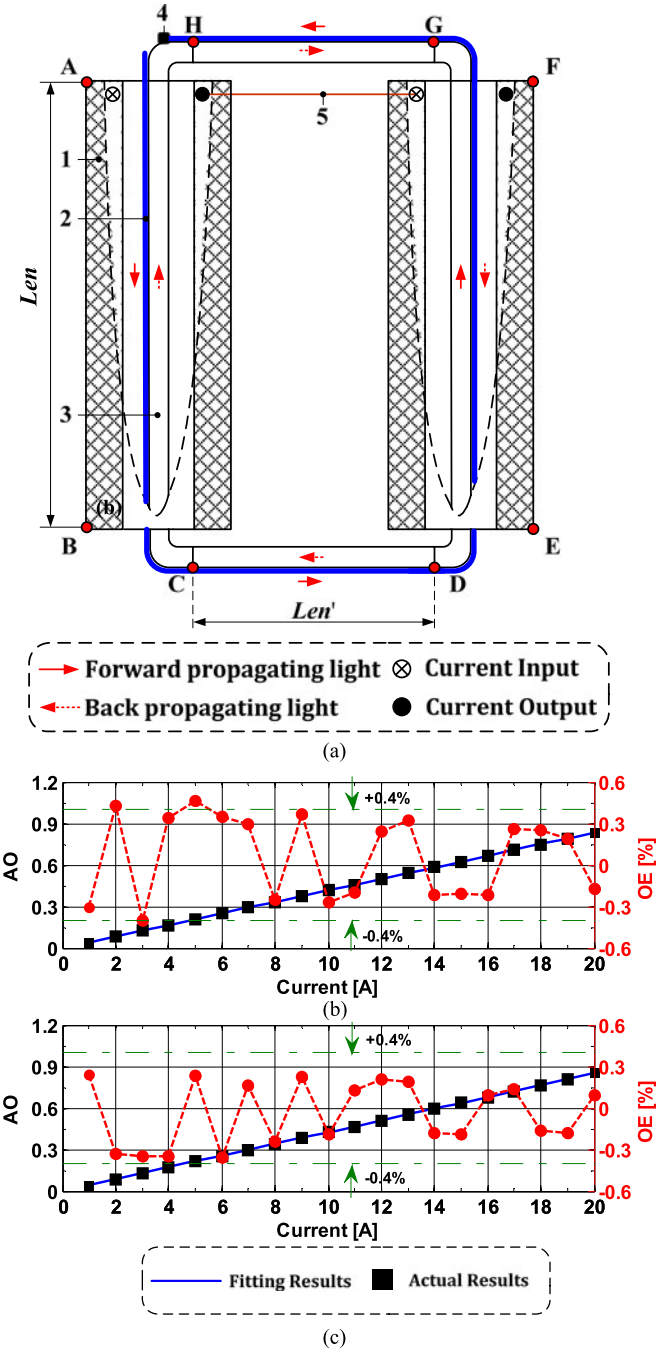

Fig. 7. Reference sensor configuration and the test results at 20 °C. (a) Reference sensor configuration. (b) Test results of the reference sensor. (c) Test results of the proposed sensor.

4. Temperature Experiments

The performance of stray current sensor with the all-side CSF is evaluated with reference to that without the CSF, and the detailed configuration of the reference sensor is shown in Fig. 7(a). For these two sensors, the most of the design parameters are the same except for the installation methods of sensing fibers, and the sensing fibers are both the low birefringent fibers (Oxford Electronics Co. Ltd., model LB 1550-125). The numbers of turns of sensing fiber are both only

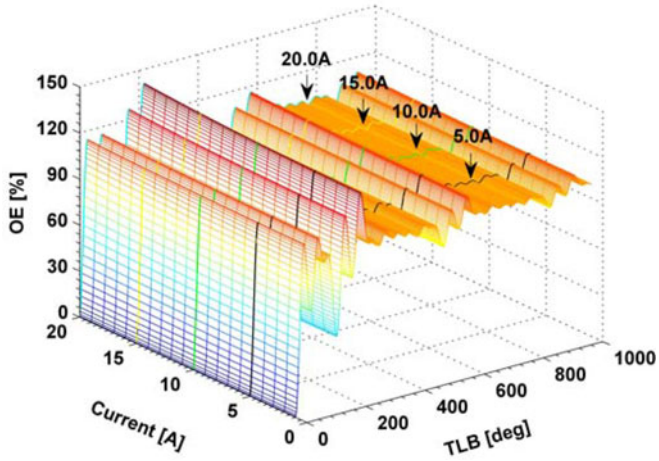

Fig. 8. Output error of the sensor without the CSF in the range of TLB from 0 deg to 1000 deg.

one. It means that the intrinsic linear birefringence of sensing fiber can be neglected. Moreover, for the reference sensor, the circular birefringence can be approximated to zero because the sensing fiber is not twisted. According to the test method presented in [3], the sensitivity of the reference sensor is about 0.0416 /A at 20 °C, which is shown in Fig. 7(b), and the sensitivity of the proposed sensor is about 0.0424 /A at 20 °C, which is shown in Fig. 7(c). Fig. 7(b) and (c) also show the measurement error curves. It can be found that the maximum error is obtained at the low current that is not greater than 5.0 A. And the maximum error is about 0.46% for the reference sensor while it is about -0.37% for the proposed sensor. It indicates that the proposed sensor has a better accuracy than the reference sensor at the low current. In addition, the effect of the TLB on the OE of reference sensor is simulated, which is shown in Fig. 8. It can be found that the OE is great in the range of the TLB from 0 deg to 1000 deg. For example, the maximum OE is about 135.04% at 5 A, 136.03% at 10 A, 137.79% at 15 A, and 140.49% at 20 A, respectively.

The temperature experiments are conducted for these two sensors. In these experiments, the central wavelength of the SLD source (EXFO Co. Ltd., model FLS-2200) is about 1550 nm. Its 3 dB spectral width is about 56 nm. The extinction ratio of the polarizer is about 35 dB. The coupling ratio of the coupler is about 50:50. The OPM are also produced by EXFO Co. Ltd. (model PM-1623). Moreover, the experiment temperature is in the range from 0 °C to 30 °C. The platinum resistance is applied as the temperature sensor, and its detection accuracy is about 0.2% in the range from 0 °C to 30 °C. The measurement result of a digital multimeter (Agilent Co. Ltd., model U3402A) is used as the standard value of the experiment current. It is noted that the DC current accuracy of this multimeter is about 0.05% while the measuring range higher limit is 12 A. And the DC voltage accuracy is about 0.012% while the measuring range lower limit is 120 mV. If the experiment current is greater than 12 A, a precision shunt (type 25A/250mV) should be required. In the sensor head, for sections AB and EF, the length of the cylindrical rod is about 1024 mm while the number of curve spirals is about 35. For sections CD and HG, the two parameters are about 876 mm and 28, respectively.

Four temperature experiments have been conducted. And these experimental results are shown in Fig. 9. In the first temperature experiment, the standard value of the experiment current is about 5.0 A. When the sensor without CSF is applied, the measured current curve is shown as Fig. 9(a), which is within the range from 4.905 A to 5.389 A, and the maximum measurement error is about 7.77%. Moreover, when the sensor with all-side CSF is applied, the measured current curve is shown as Fig. 9(b), which is within the range from 4.992 A to 5.013 A, and the corresponding measurement error is within the range from -0.17% to 0.26%. In the second experiment, the standard value is about 10.0 A. And the experiment results are shown in Fig. 9(c) and (d). For the first case, the measured current is in the range from 9.872 A to 10.749 A, and the maximum error is

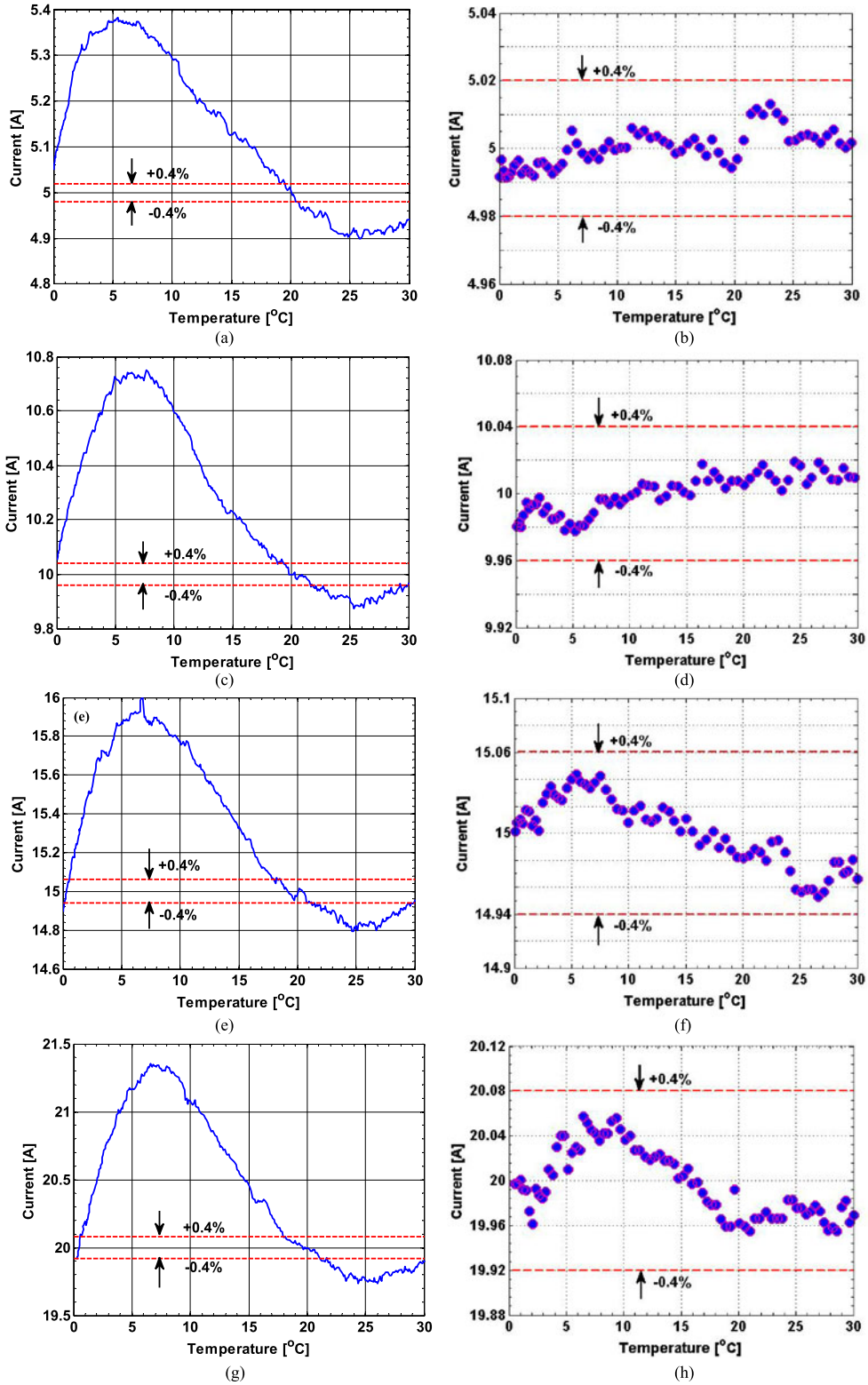

Fig. 9. Temperature experiment results. (a) Sensor without CSF at 5.0 A. (b) Sensor with all-side CSF at 5.0 A. (c) Sensor without CSF at 10.0 A. (d) Sensor with all-side CSF at 10.0 A. (e) Sensor without CSF at 15.0 A. (f) Sensor with all-side CSF at 15.0 A. (g) Sensor without CSF at 20.0 A. (h) Sensor with all-side CSF at 20.0 A.

about 7.49%. For the second case, the measured current is within the range from 9.978 A to 10.019 A. And the corresponding error is within the range from -0.225% to 0.191%. In the third experiment, the standard value is about 15.0 A. And the experiment results are shown in Fig. 9(e) and (f). For the first case, the measured current is in the range from 14.794 A to 15.998 A, and the maximum error is about 6.65%. For the second case, the measured current is within the range from 14.953 A to 15.044 A. And the corresponding error is within the range from -0.31% to 0.29%. In the last experiment, the standard value is about 20.0 A, and the experiment results are shown in Fig. 9(g) and (h). For the first case, the measured current is in the range from 19.737 A to 21.355 A, and the maximum error is about 6.78%. For the second case, the measured current is within the range from 19.955 A to 20.057 A, and the corresponding error is within the range from -0.23% to 0.29%. According to these above experiment results, the measurement errors are all not larger than 0.4% based on the proposed sensor with all-side CSF. Thus, it indicates that this sensor with all-side CSF has the good performance in the varying temperature condition.

5. Conclusion

In this paper, the stray current sensor based on an all-side CSF is firstly proposed. And the Jones matrix of sensor head is derived based on geometric rotation effect. The output representation of the proposed stray current sensor is also obtained. Moreover, the effect of the characteristic parameters of sensor head on the output error is evaluated, and the genetic algorithm is applied to optimize these characteristic parameters in the range of the temperature-induced linear birefringence from 0 deg to 1000 deg. The optimization results include: $Len = 1024$ mm, $Len' = 876$ mm, $\kappa = 35$ and $\kappa' = 28$. The temperature experiments are conducted to test the performance of the proposed stray current sensor with reference to that without CSF, and the experiment current is 5.0 A, 10.0 A, 15.0 A and 20.0 A, respectively. The experiment results indicate that the measurement error of the proposed stray current sensor is not larger than 0.4%, which can be suit for the stray current measurement in an urban rail transit system. The results can also provide reference for the elimination of the temperature-induced linear birefringence in the interferometer OFCS and the polarization-interference-based fiber vibration sensor.

Acknowledgment

The authors wish to thank the anonymous reviewers for their valuable suggestions.

References

[1] Y. Zhao, F. Zhou, F. Xu, and Y. Q. Lu, "A heterodyne optical fiber current sensor based on a nanowire-grid in-line polarizer," *IEEE Photon. J.*, vol. 4, no. 5, pp. 1288–1294, Oct. 2012.
[2] H. Zhang *et al.*, "Temperature and vibration robustness of reflecting all-fiber current sensor using common single-mode fiber," *J. Lightw. Technol.*, vol. 32, no. 22, pp. 3709–3715, Nov. 2014.
[3] S. Y. Xu, W. Li, F. F. Xing, and Y. Q. Wang, 'Polarimetric current sensor based on polarization division multiplexing detection," *Opt. Exp.*, vol. 22, no. 10, pp. 11985–11994, 2014.
[4] D. N. Huang, S. Srinivasan, and J. E. Bowers, "Compact Tb doped fiber optic current sensor with high sensitivity," *Opt. Exp.*, vol. 23, no. 23, pp. 29993–29999, 2015.
[5] P. Wei, C. Cheng, and T. T. Liu, "A photonic transducer-based optical current sensor using back-propagation neural network," *IEEE Photon. Technol. Lett.*, vol. 28, no. 14, pp. 1513–1516, Jul. 2016.
[6] S. Y. Xu, W. Li, Y. Q. Wang, and F. F. Xing, "Effect and elimination of alignment error in an optical fiber current sensor," *Opt. Lett.*, vol. 39, no. 16, pp. 4751–4754, 2014.
[7] G. M. Müller, W. Quan, M. Lenner, L. Yang, A. Frank, and K. Bohnert, "Fiber-optic current sensor with self-compensation of source wavelength changes," *Opt. Lett.*, vol. 41, no. 12, pp. 287–2870, 2016.
[8] K. Bohnert, P. Gabus, J. Kostovic, and H. Brändle, "Optical fiber sensors for the electric power industry," *Opt. Laser Eng.*, vol. 43, no. 3–5, pp. 511–526, 2005.
[9] L. H. Wang, G. J. Wei, J. F. Ji, and J. Liu, "Statistical modeling of fiber optic current transducer," *Measurement*, vol. 92, pp. 288–294, 2016.
[10] K. Bohnert, H. Brändle, M. G. Brunzel, P. Gabus, and P. Guggenbach, "Highly accurate fiber-optic DC current sensor for the electrowinning industry," *IEEE Trans. Ind. Appl.*, vol. 43, no. 1, pp. 180–187, Jan./Feb. 2007.
[11] G. Cui, Z. L. Li, C. Yang, and M. Wang, "The influence of DC stray current on pipeline corrosion," *Petroleum Sci.*, vol. 13, no. 1, pp. 135–145, 2016.

[12] S. Y. Xu, W. Li, and Y. Q. Wang, "Effects of vehicle running mode on rail potential and stray current in DC mass transit systems," *IEEE Trans. Veh. Technol.*, vol. 62, no. 8, pp. 3569–3580, Oct. 2013.
[13] K. Bohnert, P. Gabus, J. Nehring, and H. Brändle, "Temperature and vibration insensitive fiber-optic current sensor," *J. Lightw. Technol.*, vol. 20, no. 2, pp. 267–276, Feb. 2002.
[14] N. Peng *et al.*, "Fiber optic current sensor based on special spun highly birefringent fiber," *IEEE Photon. Technol. Lett.*, vol. 25, no. 17, pp. 1668–1671, Sep. 2013.
[15] G. M. Müller, X. Gu, L. Yang, A. Frank, and K. Bohnert, "Inherent temperature compensation of fiber-optic current sensors employing spun highly birefringent fiber," *Opt. Exp.*, vol. 24, no. 10, pp. 11164–11173, 2016.
[16] M. Segura *et al.*, "Low birefringence measurement and temperature dependence in meter-long optical fibers," *J. Lightw. Technol.*, vol. 33, no. 12, pp. 2697–2702, Jun. 2015.
[17] C. D. Perciante and J. A. Ferrari, "Cancellation of bending-induced birefringence in single-mode fibers: Application to Faraday sensors," *Appl. Opt.*, vol. 45, no. 9, pp. 1951–1956, 2006.
[18] E. M. Frins and W. Dultz, "Rotation of the polarization plane in optical fibers," *J. Lightw. Technol.*, vol. 15, no. 1, pp. 144–147, Jan. 1997.
[19] P. Tantaswadi, "Simulation of birefringence effects in reciprocal fiber-optic polarimetric current sensor," in *Proc. SPIE*, Bellingham, WA, USA, 2001, pp. 158–164.
[20] I. M. Nascimento, A. C. S. Brígida, J. M. Baptista, J. C. W. A. Costa, M. A. G. Martinez, and P. A. S. Jorge, "Novel optical current sensor for metering and protection in high power applications," *Instrum. Sci. Technol.*, vol. 44, no. 2, pp. 148–162, 2016.
[21] F. C. Strong, "Faraday's laws in one equation," *J. Chem. Educ.*, vol. 38, no. 2, p. 98, 1961.
[22] G. Rudolph, "Convergence analysis of canonical genetic algorithms," *IEEE Trans. Neural Netw.*, vol. 5, no. 1, pp. 96–101, Jan. 1994.
[23] M. Srinivas and L. M. Patnaik, "Genetic algorithms: A survey," *Computer*, vol. 27, no. 6, pp. 17–26, Jun. 1994.
[24] S. K. Teegala and S. K. Singal, "Optimal costing of overhead power transmission lines using genetic algorithms," *Int. J. Elect. Power*, vol. 83, pp. 298–308, 2016.